Electronic supplementary information

Equilibrium unconstrained low-temperature CO$_2$ conversion on doped gallium oxides by chemical looping

Keke Kang[a], Sota Kakihara[a], Takuma Higo[a], Hiroshi Sampei[a], Koki Saegusa[a], Yasushi Sekine*[a]

*Correspondence to: Yasushi SEKINE: ysekine@waseda.jp

This file includes:
> Supplementary text
> Figures S1 to S20
> Tables S1 to S4

Supplementary text

Material and method

Material preparation

Ga_2O_3, $NiGa_2O_4$, $CuGa_2O_4$, $CoGa_2O_4$ used in this study were prepared by a complex polymerization method. Firstly, the stoichiometric precursors (Kanto Chemical Co. Inc.) of $Cu(NO_3)_2 \cdot 3H_2O$ (when used), $Co(NO_3)_2 \cdot 6H_2O$ (when used) , $Ni(NO_3)_2 \cdot 6H_2O$ (when used) and $Ga(NO_3)_3 \cdot nH_2O$ were dissolved in pure water, then excess citric acid and ethylene glycol (Kanto Chemical Co. Inc.) with molar ratio of metal ion: citric acid: ethylene glycol = 1:3:3 were put into the solutions. Afterward, the solutions were stirred in a water bath at 353 K for 18 h, and then dried with stirring at 573 K. After that, the obtained solid mixtures were moved into muffle furnace, pre-calcined at 673 K for 2 h and calcined at 1123 K for 10 h. Finally, the target materials were successfully prepared.

Evaluation of maximum CO_2 conversion

The maximum CO_2 conversion of the oxidation step (equation 5) was measured on a thermogravimetric analyzer (TG-50A; Shimadzu Corp.). The oxide material was firstly pre-reduced by 40% H_2 (Ar balance), and then oxidized by CO-CO_2 mixed gas (Ar balance) with certain CO/CO_2 ratio. If signal for weight increase of the material was captured, it would be deemed that the oxidation reaction (equation 5) could forward proceed (from left to right) with that CO/CO_2 ratio. In this situation, CO-CO_2 mixed gas with higher CO/CO_2 ratio would be introduced, and then the above operations would be repeated until weight decrease of the material observed. The CO/CO_2 ratio just before weight starting to decrease was defined as the maximum CO_2 conversion of the oxide material.

RWGS-CL cycle test

RWGS-CL cycle test was performed on a thermogravimetric apparatus (TG-50A; Shimadzu Corp.) using 30 mg of the as prepared oxide material. After rising to pre-set temperatures in Ar atmosphere, $NiGa_2O_4$ and $CuGa_2O_4$ were sufficiently pre-reduced by 40% H_2 (Ar balance) at 973 K until all the oxides can participate in the redox cycles and the following cycles reaching stable. However, although $CoGa_2O_4$ were pre-

2

reduced at 1073 K (the low reduction rate is relatively low at 973 K) with more than two oxygen atoms were reduced, not all the oxides can participate in the redox cycles. It is shown in Fig. S5 that the reduction amounts of $CoGa_2O_x$ increase cycle by cycle, and the XRD peaks for unreacted $CoGa_2O_4$ are always remained after reduction and even after 5 cycles oxidation in Fig. S6. These confirm that $CoGa_2O_x$ didn't reach stable after pre-reduction. Deeper pre-reduction at high temperature will aggregate the particles and shrink the surface area, thereby further decrease the oxidation rate. Therefore, we suppose $CoGa_2O_x$ is not so proper material for RWGS-CL and keep the pre-reduction condition here.

After the pre-reduction, the temperature was respectively changed to 873 K, 923 K, 973 K, 1023 K and 1073 K in Ar atmosphere for the following isothermal cycles. And then the oxides were re-oxidized under different oxidation conditions (10% CO_2; 90% CO-10% CO_2). Both oxidation step with CO_2 and with CO+CO_2 were stopped until no fast increase of the sample weight could be observed, which is determined by the differential of the weight change. Then the oxidized materials were reduced by 40% H_2 (Ar balance) for 30 min, and this is defined as reduction step. And a set of reduction and oxidation step was defined as one cycle of isothermal RWGS-CL. The total flow rate was set constant to 100 mL min^{-1}. As calculated according to following equation S1, the amounts of reduction and oxidation (redox) were defined as the amounts of oxygen atoms released or restored in each step.

$$\text{Reduction or Oxidation (Redox) amount [mmol g}^{-1}] = \frac{|\Delta m|}{m_{\text{sample}} \times M_O} \quad \text{(S1)}$$

In this equation, Δm / mg, m_{sample} / g and M_O / g mol^{-1} respectively represent the change of sample weight during each step, the initial sample weight, and molar mass of oxygen atom. The average CO_2 splitting rate was defined as shown in equation S2.

$$\text{Average CO}_2 \text{ splitting rate [mmol g}^{-1} \text{ min}^{-1}] = \frac{\text{Amount of oxidation}}{\Delta t} \quad \text{(S2)}$$

Therein, Δt / min represents the time necessary to complete CO_2 oxidation.

H$_2$-TPR and CO$_2$-TPO

H$_2$ temperature-programmed reduction (H$_2$-TPR) and CO$_2$ temperature-

programmed oxidation (CO_2-TPO) were conducted on TG-50A (Shimadzu Corp.) aiming to investigate the redox properties of the oxides. For H_2-TPR, after H_2 pretreatment and re-oxidation with $CO+CO_2$ at 973 K, the materials were cooled down to 573 K in Ar atmosphere and then risen to 1073 K with heating rate of 4 K min^{-1} in 10% H_2 flow. The reacted H_2 amount is detected by the mass loss of the oxide materials.

Thereafter, CO_2-TPO was conducted with the reduced oxygen carriers resulted from the H_2-TPR. After the materials were cooled down to 573 K in Ar atmosphere after H_2-TPR, they were oxidized by 10% CO_2 with a heating rate of 4 K min^{-1} from 573 K to 1073 K. The reacted CO_2 amount is detected by the gained mass of the oxide materials. Consumed H_2 and CO_2 amounts during the H_2-TPR and CO_2-TPO experiment were calculated by the following equation:

$$H_2 \text{ or } CO_2 \text{ consumption rate} \left[\text{mmol g}^{-1}\text{ min}^{-1}\right] = \frac{\text{Amount of reduction/oxidation}}{\Delta t} \quad \text{(S3)}$$

Structural characterizations (XRD, TEM-EDX, BET and *in situ* XAFS)

To investigate the crystal structure of the prepared materials, powder X-ray diffraction (XRD) measurements were conducted using an X-ray diffractometer (Smart Lab-III; Rigaku Corp.) with Cu-$K\alpha$ radiation at 40 kV and 40 mA.

The morphology and element distribution of $NiGa_2O_4$ were investigated by a scanning transmission electron microscope with an energy-dispersive X-ray spectrometer (STEM-EDX; JEOL JEM 2100F).

The specific surface area was calculated from nitrogen adsorption isotherm at 77 K by the Brunauer−Emmett−Teller (BET) method (Gemini VII 2390a; Micromeritics Instrument).

In situ X-ray adsorption fine structure (*in situ* XAFS) measurement for Ga and Ni K-edge was conducted at the beamline BL14B2 of SPring-8 using transmission mode. Quantificational $NiGa_2O_4$ powder and boron nitride (BN) were mixed and crushed together evenly, and pressed into a 10 mm pellet to put in *in situ* cell. The size of the beam that can transmit the sample pellet is 1 (vertical) mm × 5.0 (horizontal) mm. First, the sample pellet was ramped up to 973 K in N_2 flow and then pre-reduced by 40% H_2

for 90 min at 973 K. After pre-reduction treatment, the oxidation by 10% CO_2 of the sample pellet was conducted for 30 min at 973 K. Then another reduction by 40% H_2 for 30 min, which is followed by the oxidation of the mixing gas of 80% CO and 20% CO_2. The XAFS spectra were captured regularly during all the reduction and oxidation steps. Gas lines were cleaned by purging N_2 for 10 min before changing to another gas. N_2 was used as balance gas and the total flow rate is kept as 100 mL min^{-1} during the whole process.

Computational details

   Density functional theory (DFT) calculations were performed by the Vienna Ab initio Simulation Package (VASP) 6.3.1 [*Kresse 1993*] [*Kresse 1996*], which can represent the core-valence electrons by using a projector augmented wave (PAW) method [*Blochl 1994*] [*Kresse 1999*]. Electron exchange and correlation were described by the generalized gradient approximation (GGA) of Perdew-Burke-Ernzerhof (PBE) [*Perdew 1996*]. And we employed a plane-wave cutoff energy as 400 eV. Also, the total energy convergence of structure optimization was set to 10^{-5} eV. All calculations were considered the spin polarization and van der Waals interactions by using DFT-D3 proposed by Grimme [*Grimme 2010*].

   X-ray absorption near edge structure (XANES) was simulated by using CASTEP code [*Clark 2005*] integrated in the Materials Studio software package. CASTEP calculations were also employed the GGA-PBE as an exchange -correlation function. Cutoff energy was set to 400 eV and self-consistent field (SCF) convergence tolerance was set to 10^{-6} eV/atom. Also, ($2\times2\times2$) Monkhorst-Pack k-point mesh was used for SCF calculations and XANES simulations. This simulation was also considered the van der Walls interaction using DFT-D3 as well. The calculated XANES spectra were smoothed and shifted because of high energy resolution and low accuracy of absolute energy on DFT calculations. The smoothing and shift parameters were decided by adjusting calculated spectrum of Ni metal to measured spectrum of that between -10 to 20 eV of absorption edge.

References:

[Kresse 1993] G. Kresse and J. Hafner, *Phys. Rev. B*, **47** (1993) 558–561.

[Kresse 1996] G. Kresse and J. Furthmüller, *Phys. Rev. B*, **54** (1996) 11169–11186.

[Blochl 1994] P.E. Blöchl, *Phys. Rev. B*, **50** (1994) 17953–17979.

[Kresse 1999] G. Kresse and D. Joubert, *Phys. Rev. B*, **59** (1999) 1758–1775.

[Perdew 1996] J. P. Perdew, K. Burke and M. Ernzerhof, *Phys. Rev. Lett.*, **77** (1996) 3865–3868.

[Grimme 2010] S. Grimme, J. Antony, S. Ehrlich and S. Krieg, *J. Chem. Phys.*, **132** (2010) 154104.

[Clark 2005] S. J. Clark, M. D. Segall, C. J. Pickard, P. J. Hasnip, M. I. J. Probert, K. Refson and M. C. Payne, *Z. Kristallogr.*, **220** (2005) 567–570.

Ozawa−Flynn−Wall kinetics analysis

Ozawa−Flynn−Wall (OFW) kinetics analysis is a model-free (isoconversional) method, whose kinetics parameters can be obtained through thermogravimetric curves [*Flynn 1966*] [*Ozawa 1965*]. The activation energy (E_a) can be obtained from the conversion (α) of oxides and different constant heating rates (β).

The conversion (α) of the oxides was defined as the following equation S4, where m_i is the initial weight (the weight of oxides before reaction), m_t is the weight at the time t and m_f is the final weight (the weight of oxides when completing the reaction).

$$\alpha = \frac{m_t - m_i}{m_f - m_i} \qquad \text{(S4)}$$

If the investigated sample with the same α, the dependence of β and E_a can be obtained by the OFW equation S5, showing as a straight line. That is to say, E_a can be calculated from the slop of the straight line from $\log \beta$ versus $1/T$.

$$\log \beta + 0.4567 \frac{E_a}{RT} = \text{constant} \qquad \text{(S5)}$$

In this work, thermogravimetric apparatus (TG-50A; Shimadzu Corp.) was used to obtain the kinetics parameters. To figure out why $NiGa_2O_x$ can show high CO_2 splitting rate even under 90% concentration of CO, $CuGa_2O_x$ was investigated as a reference. The experiments were conducted by separately oxidize the samples with 10% CO_2 and reduce them with 90% CO. For the CO_2 oxidation, after the pre-reduction treatment by 40% H_2 at 973 K and cooling down to room temperature, samples were oxidized by 10% CO_2 with the temperature heating up to 1123 K, and the heating rate (β) for $NiGa_2O_x$ is 5, 10 ,15, 20 K min^{-1} and for $CuGa_2O_x$ is 5, 10, 20 K min^{-1}. Similarly,

for the CO reduction, after the pre-reduction treatment by 40% H_2, re-oxidation by 10% CO_2 at 973 K, and cooling down to room temperature, the oxidized samples were reduced by 90% CO with the temperature heating up to 1123 K, and the heating rate (β) for $NiGa_2O_x$ is 2, 5, 10, 20 K min^{-1} and for $CuGa_2O_4$ is 5, 10, 20 K min^{-1}.

References:
[Flynn 1966] J. H. Flynn and L. A. Wall, *J. Polym. Sci. B Polym. Phys.*, 1966, **4**, 323-328.
[Ozawa 1965] T. Ozawa, *Bull. Chem. Soc. Jpn.*, 1965, **38**, 1881-1886.
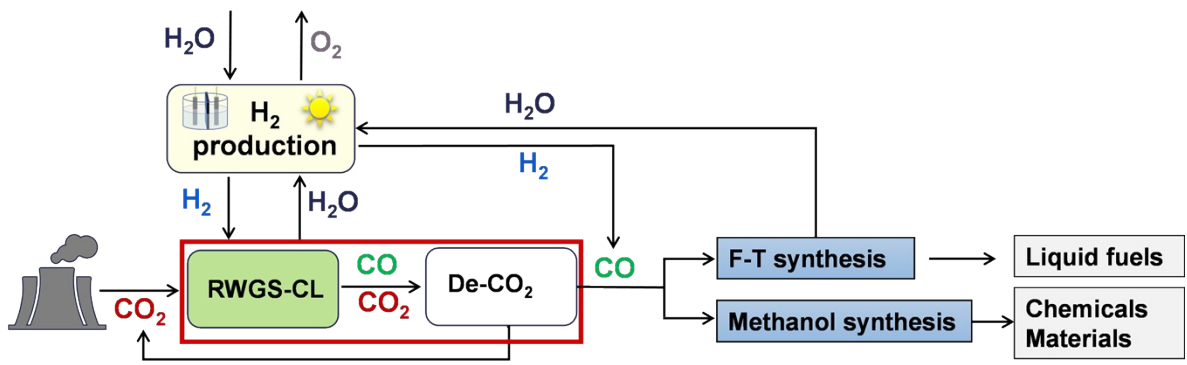
Fig. S1 The overall route of carbon-neutral and sustainable process with RWGS-CL.
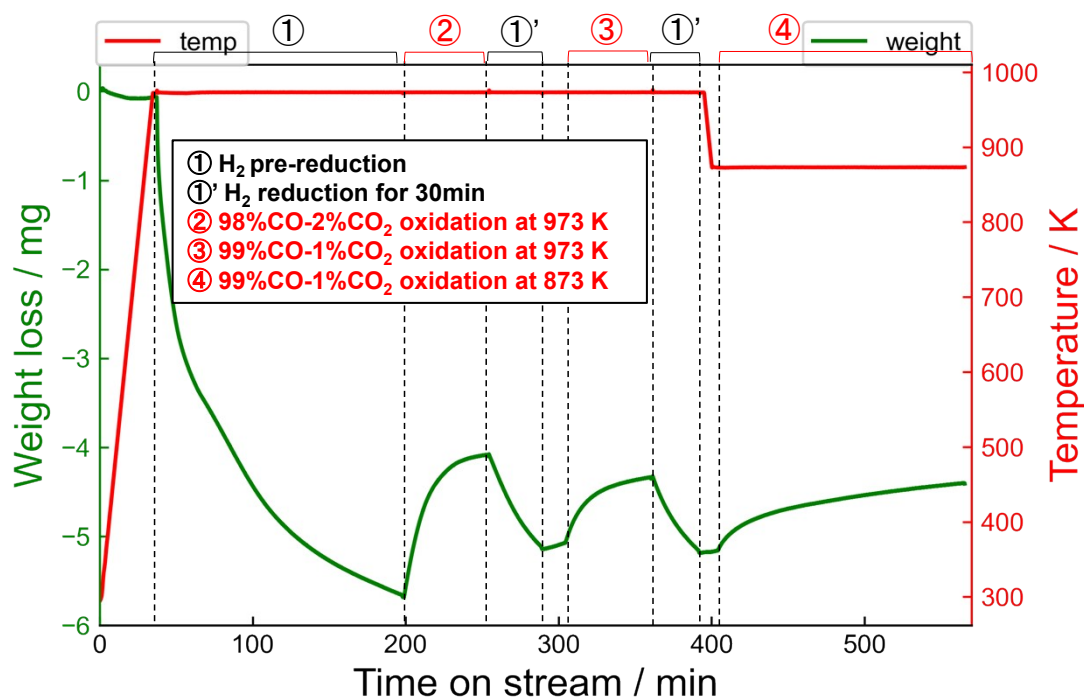
Fig. S2 The maximum CO_2 conversion evaluation of $NiGa_2O_x$ at 873 and 973 K.
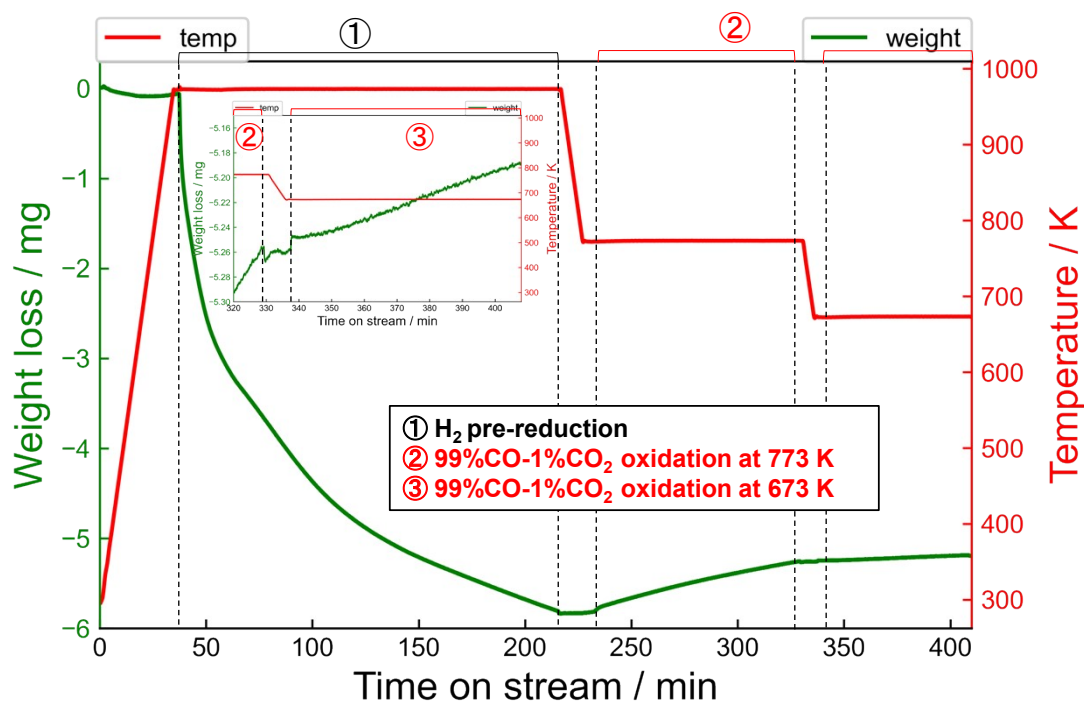
Fig. S3 The maximum CO_2 conversion evaluation of $NiGa_2O_x$ at 673 and 773 K.
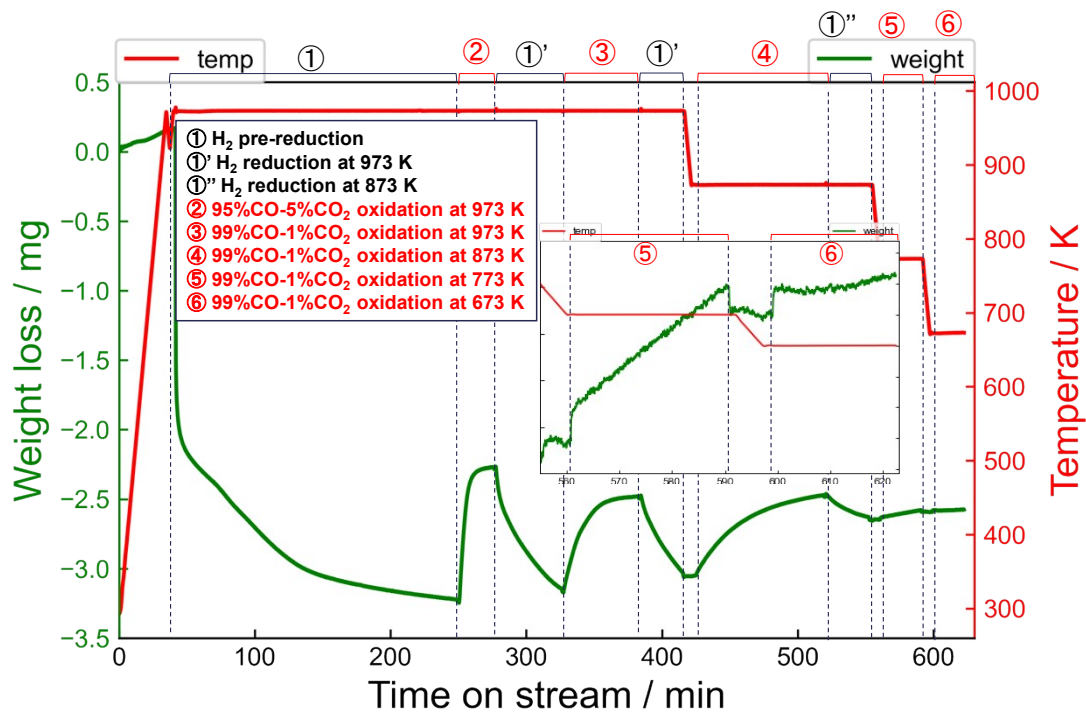
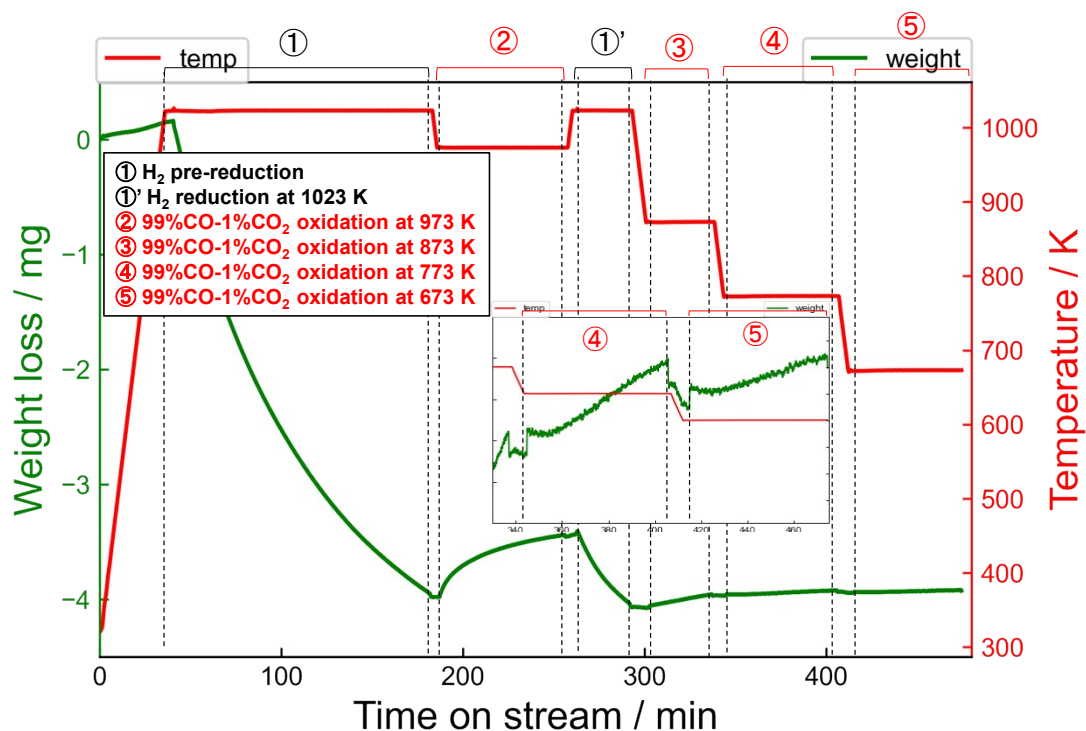Fig. S4 The maximum CO_2 conversion evaluation of $CuGa_2O_x$ at 673, 773, 873 and 973 K.

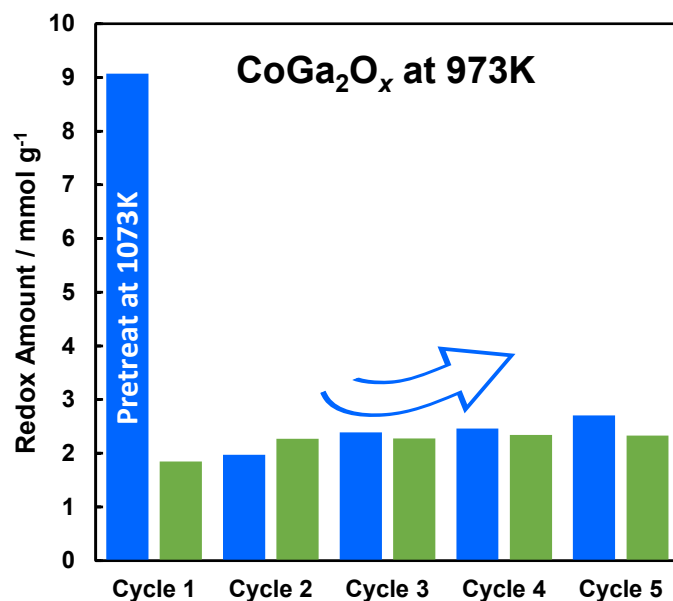Fig. S5 The maximum CO_2 conversion evaluation of $CoGa_2O_x$ at 673, 773, 873 and 973 K.

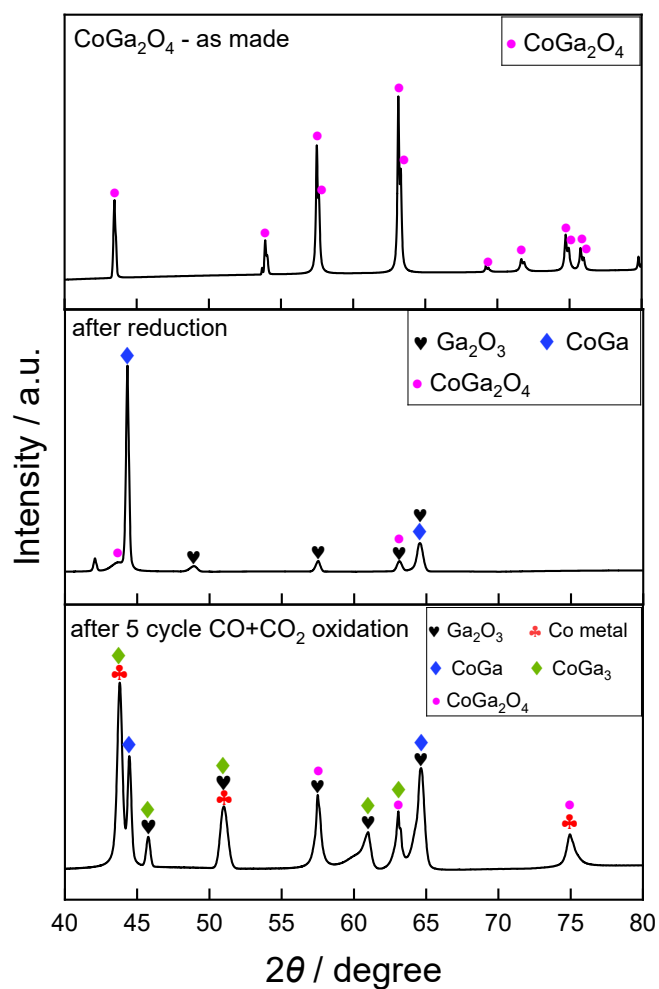Fig. S6 The redox amounts of $CoGa_2O_x$ with 90% CO-10% CO_2 as oxidation gas at 973K.

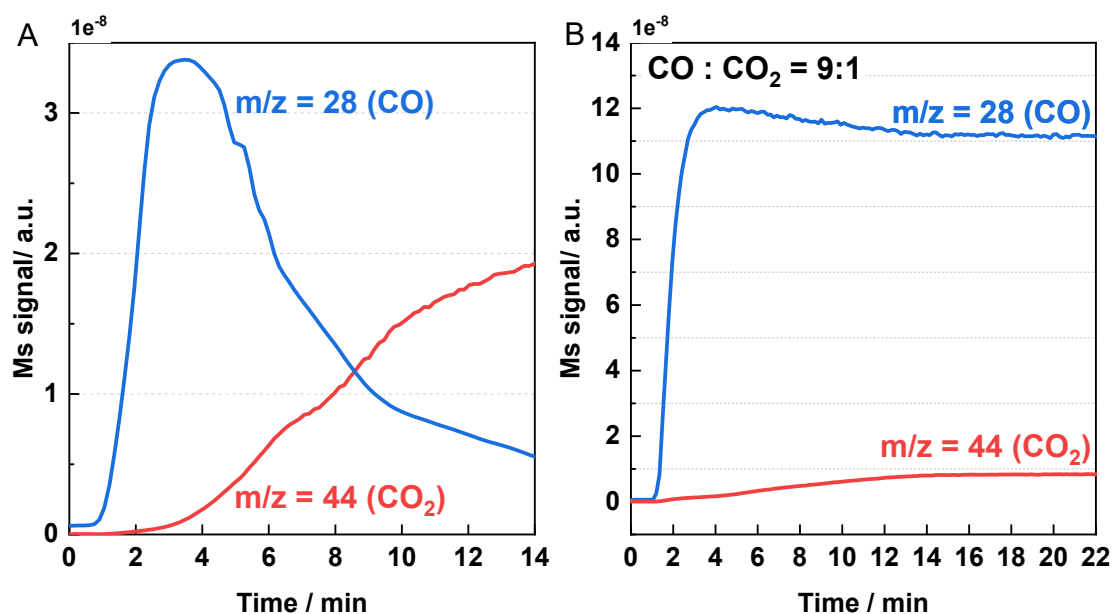Fig. S7 The XRD profiles of $CoGa_2O_x$ during RWGS-CL process.

Fig. S8 MS spectra for the outlet gas of $NiGa_2O_x$ during (A) CO_2 oxidation (B) $CO+CO_2$ oxidation at 973K.

To support the experimental results obtained by the thermogravimetric analyzer, we have conducted similar experiments using a fixed bed flow reactor equipped with a quadrupole mass spectrometer (Q-MS). Fig. S8 shows MS spectra for the outlet gas of $NiGa_2O_x$ during both CO_2 oxidation and $CO+CO_2$ oxidation at 973K, it can be seen that CO is produced without any by-products during the re-oxidation by CO_2. And we also checked carbon deposition after $CO+CO_2$ oxidation (check the amount of produced CO_2 with O_2 flowing through the sample after reaction), and the deposited carbon amount is 0.1%/g sample, which can be neglected and will not influence the result from thermogravimetric analyzer.

For the oxidation with CO_2 in Fig. S8A, in the first two minutes, there is no signal for CO_2 but a fast increase for CO, indicating high CO_2 conversion to CO of $NiGa_2O_x$. And for the oxidation with $CO-CO_2$ mixed gas with $CO:CO_2$ ratio of 9:1 in Fig. S8B, rapid increase of the signal of CO was observed immediately after the supply of $CO-CO_2$ gas, and then slowly decreases to a stable level. The peak for CO signal suggests that the forward reaction (CO production from CO_2) proceeds under $CO:CO_2$ ratio of 9:1. And the stable parts indicates that the rate of the forward and reverse reactions were balanced. These results obtained using a fixed-bed reactor set-up can well support the results obtained by thermogravimetric analyzer. Therefore, we consider that the data

shown in this paper reflects the actual kinetics of $NiGa_2O_x$, and the data obtained by our reaction set-up is sufficiently reliable and reproducible based on no by-products and neglectable carbon deposition.
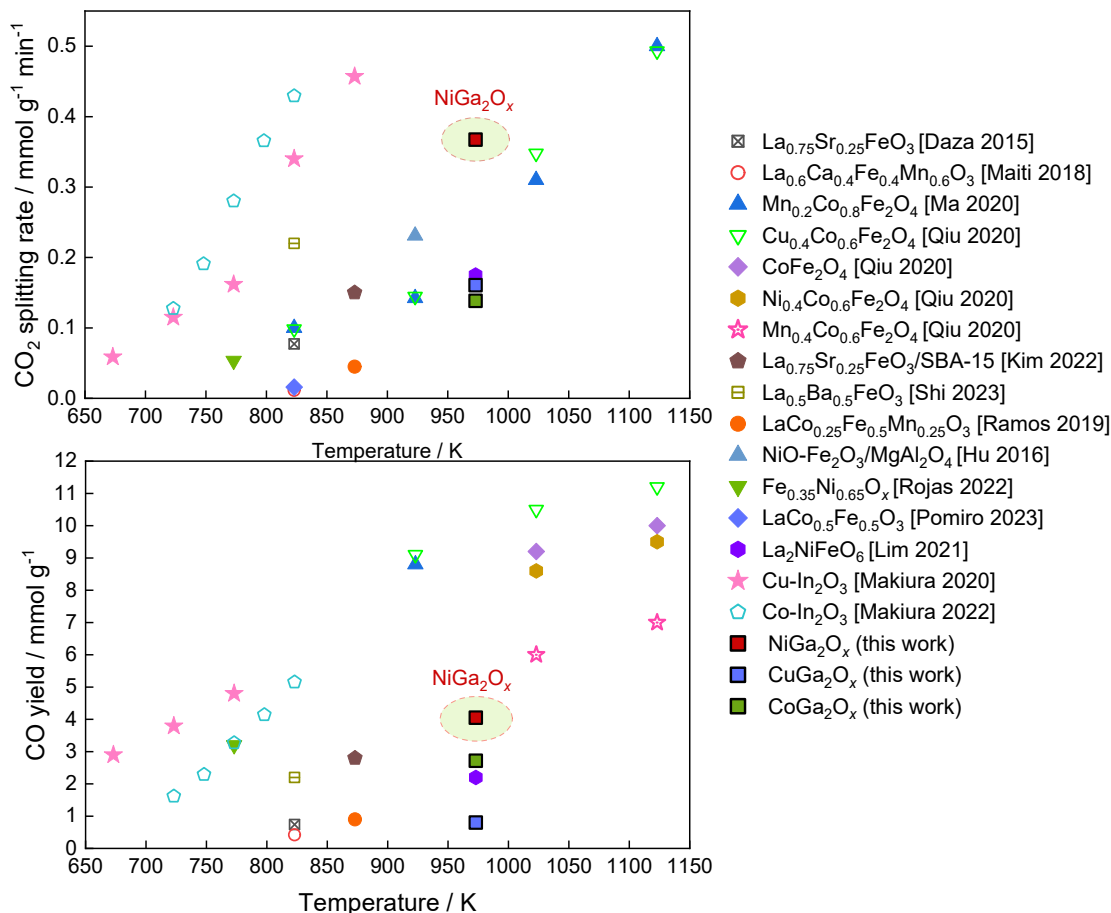
Fig. S9 Comparation of the CO$_2$ splitting rate and CO yield for RWGS-CL in present

work and in the literatures.

References:
[Daza 2015] Y. A. Daza, D. Maiti, R. A. Kent, V. R. Bhethanabotla and J. N. Kuhn, *Catal. Today*, 2015, **258**, 691-698
[Maiti 2018] D. Maiti, B. J. Hare, Y. A. Daza, A. E. Ramos, J. N. Kuhn and V. R. Bhethanabotla, *Energy Environ. Sci.*, 2018, **11**, 648-659.
[Ma 2020] L. Ma, Y. Qiu, M. Li, D. Cui, S. Zhang, D. Zeng and R. Xiao, *Ind. Eng. Chem. Res.*, 2020, **59**, 6924-6930.
[Qiu 2020] Y. Qiu, L. Ma, D. Zeng, M. Li, D. Cui, Y. Lv, S. Zhang and R. Xiao, *J. Energy Chem.*, 2020, **46**, 123-132.
[Kim 2022] Jo, Y. Kim, H. S. Lim, M. Lee, D. Kang and J. W. Lee, *J. CO$_2$ Util.*, 2022, **56**, 101845.
[Shi 2023] H. Shi, V. R. Bhethanabotla and J. N. Kuhn, *J. Ind. Eng. Chem.*, 2023, **118**, 44-52.
[Ramos 2019] E. Ramos, D. Maiti, Y. A. Daza, J. N. Kuhn and V. R. Bhethanabotla, *Catal. Today*, 2019, **338**, 52-59.
[Hu 2016] J. W. Hu, L. Buelens, S. A. Theofanidis, V. Galvita, H. Poelman, G. B. Marin, *J. CO$_2$ Util.*, 2016, **16**, 8-16
[Rojas 2022] J. Rojas, E. Sun, G. Wan, J. Oh, R. Randall, V. Haribal, I.-h. Jung, R. Gupta and A. Majumdar, *ACS Sustain. Chem. Eng.*, 2022, **10**, 12252-12261.
[Pomiro 2023] F. J. Pomiro, G. G. Fouga, A. E. Bohé and G. De Micco, *J. Alloys Compd.*, 2023, **938**, 168671.
[Lim 2021] H. S. Lim, Y. Kim, D. Kang, M. Lee, A. Jo and J. W. Lee, *ACS Catal.*, 2021, **11**, 12220-12231.
[Makiura 2020] J. I. Makiura, T. Higo, Y. Kurosawa, K. Murakami, S. Ogo, H. Tsuneki, Y. Hashimoto, Y. Sato and Y. Sekine, *Chem. Sci.*, 2020, **12**, 2108-2113.
[Makiura 2022] J. I. Makiura, S. Kakihara, T. Higo, N. Ito, Y. Hirano and Y. Sekine, *Chem. Commun.*, 2022, **58**, 4837-4840.
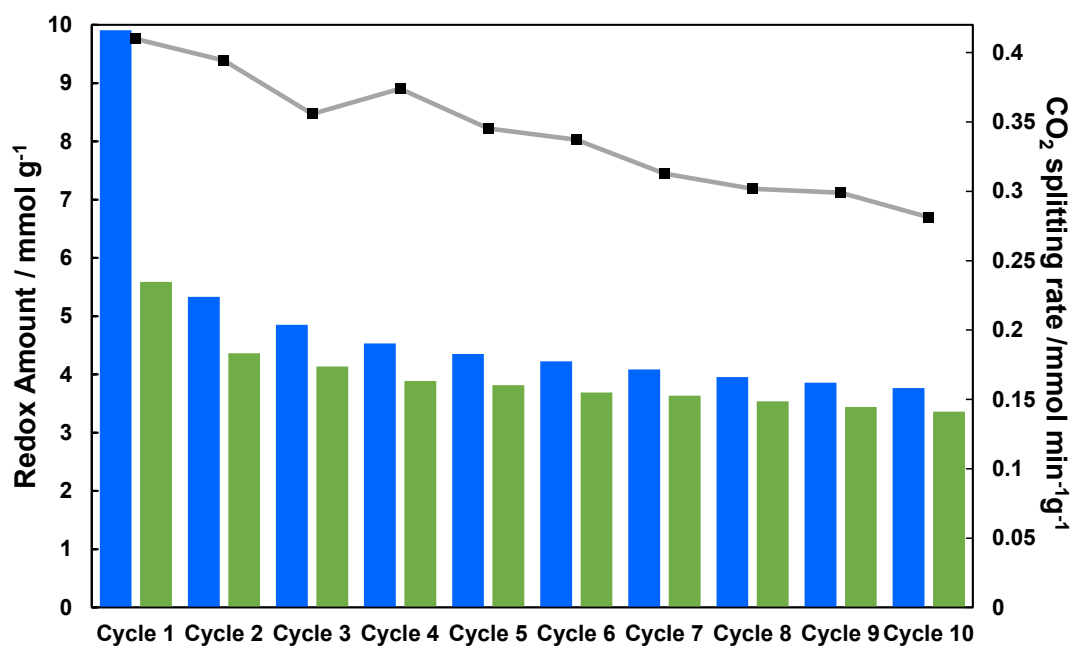
Fig. S10 Stability of NiGa$_2$O$_x$ during 10 cycles at 973K.
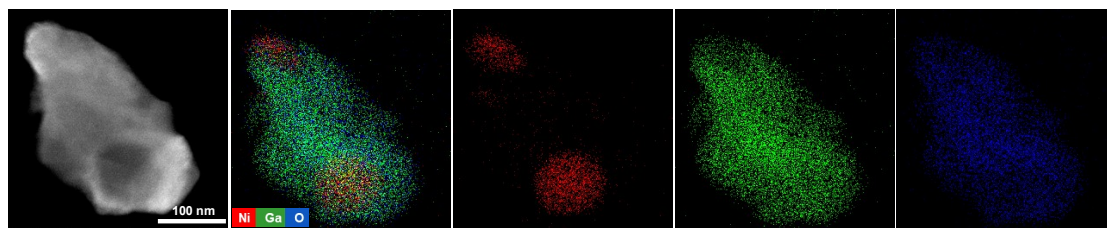

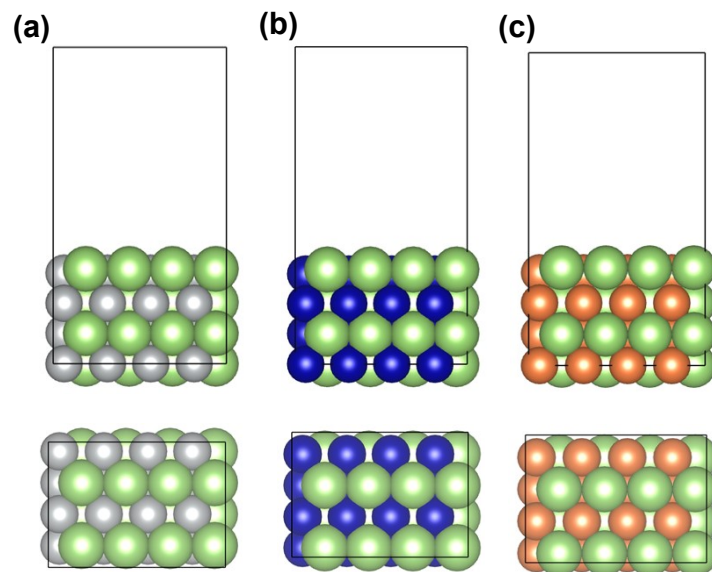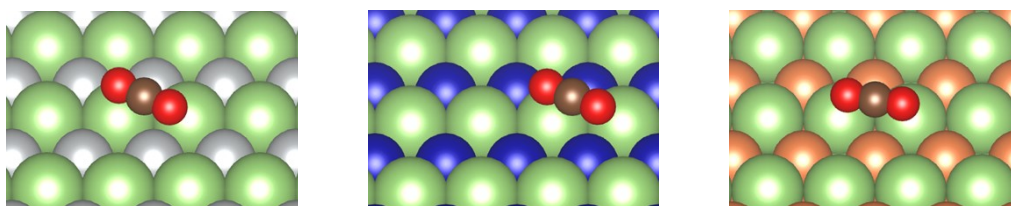Fig. S11 STEM-EDX images of NiGa$_2$O$_x$ after 10 cycle reaction.

Fig. S12 Calculation model of (a) NiGa (110), (b) CoGa (110), and (c) CuGa (110). (Ga, Ni, Co, and Cu are illustrated as green, grey, blue, and orange.)

CO_2 adsorption
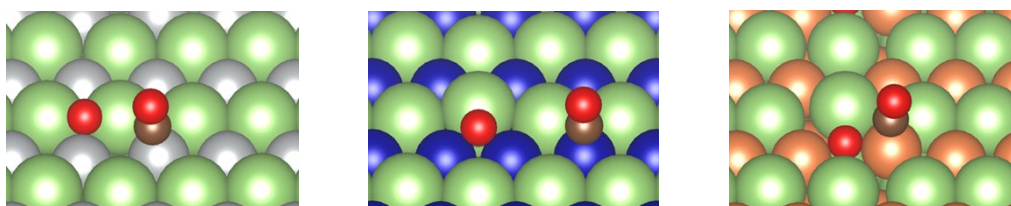

C-O dissociation

Fig. S13 Adsorption model on NiGa(110), CoGa(110), and CuGa(110). (Ga, Ni, Co, Cu, C, and O are illustrated as green, grey, blue, orange, brown, and red.)
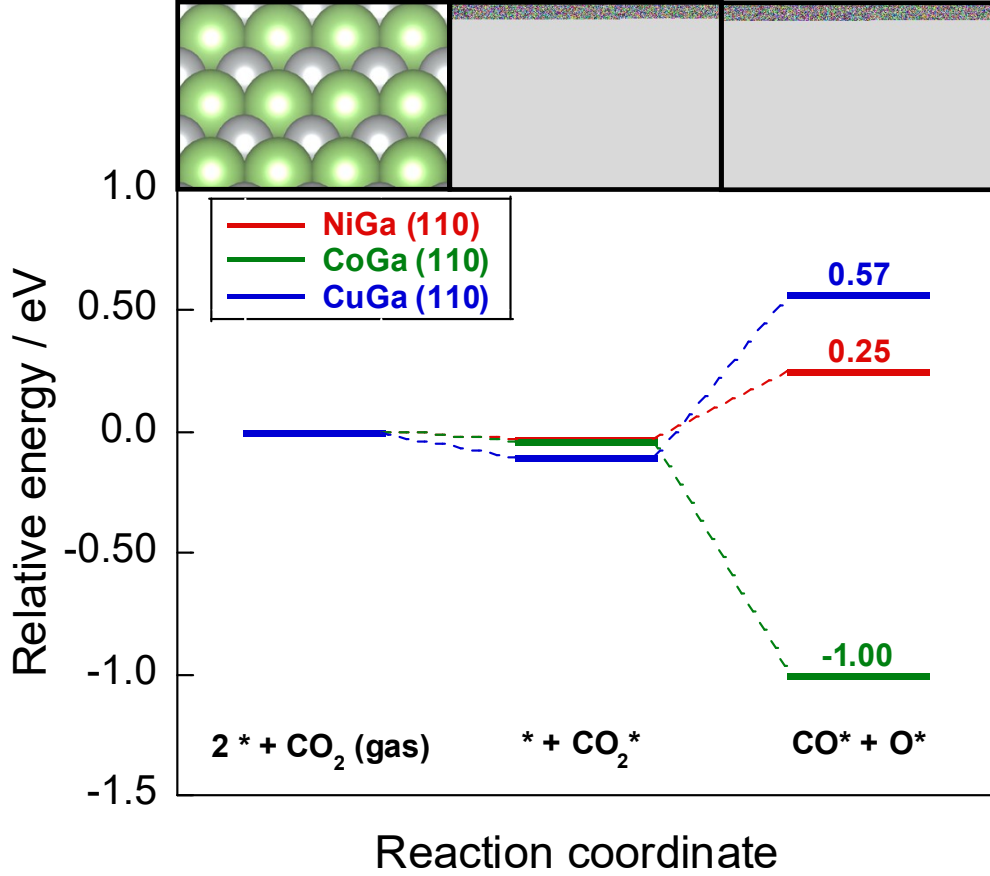
Fig. S14 Energy diagrams of CO_2 splitting on NiGa, CoGa, and CuGa surface.

To clarify the electronic structure of each alloy, NiGa, CoGa, and CuGa bulk systems were optimized by density functional theory (DFT) calculations, and the surface models of those alloys were prepared as a four-layer with a 4×4 expansion and 15 Å of vacuum layer as shown in Fig. S12. The bottom two layers were fixed during the geometry optimization. The Brillouin zone is sampled with a Γ-centered (56×56×56) and (3×4×2) Monkhorst-Pack k-point mesh for bulk model and slab model, respectively.

The adsorption energies were calculated by using the following equation.

$$\Delta E_{ad} = E(surface\ with\ adsorbate) - \{E(suface) + E(CO_2)\} \tag{1}$$

Where, $E(surface\ with\ adsorbate)$, $E(surface)$, and $E(CO_2)$ denote the total energy of alloy surface model with adsorbate, alloy surface without adsorbate, and CO_2 molecule, respectively. The isolated molecule of CO_2 was calculated in a $10 \times 10 \times 10$ Å vacuum

cubic box, and Adsorption model on NiGa (110), CoGa (110), and CuGa (110) facet is shown in Fig. S13. All surface models were depicted by the visualization for electronic and structural analysis (VESTA) [*Momma 2011*]. Energy diagram on CO_2 splitting for each alloy in Fig. S14 and the adsorption energy in Table S2 show that NiGa (110) facet brings the most moderate C-O dissociation enthalpy among these three alloy facets, which is affected by CO adsorption ability on each alloy surface. Therefore, we found out that Ni-doping material brings better CO adsorption ability than the other two, and this nature might be the main reason Ni outperformed Cu and Co as the dopant.

References:

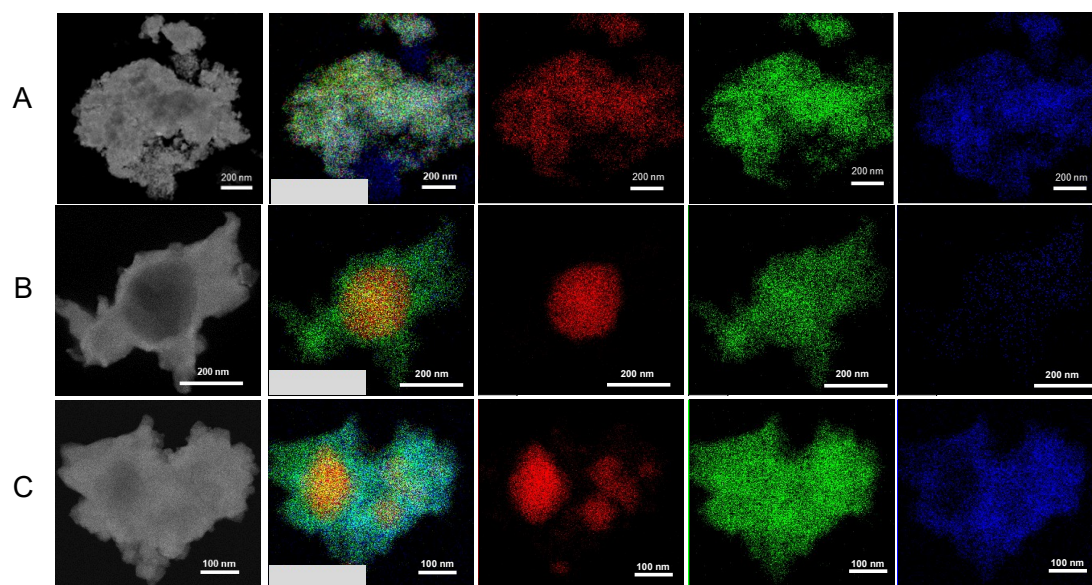[Momma 2011] K. Momma and F. Izumi, *J. Appl. Crystallogr.*, **44** (2011) 1272–1276.

Fig. S15 STEM-EDX images of NiGa$_2$O$_x$ (A) as-made (B) after reduction and (C) after CO+CO$_2$ oxidation.
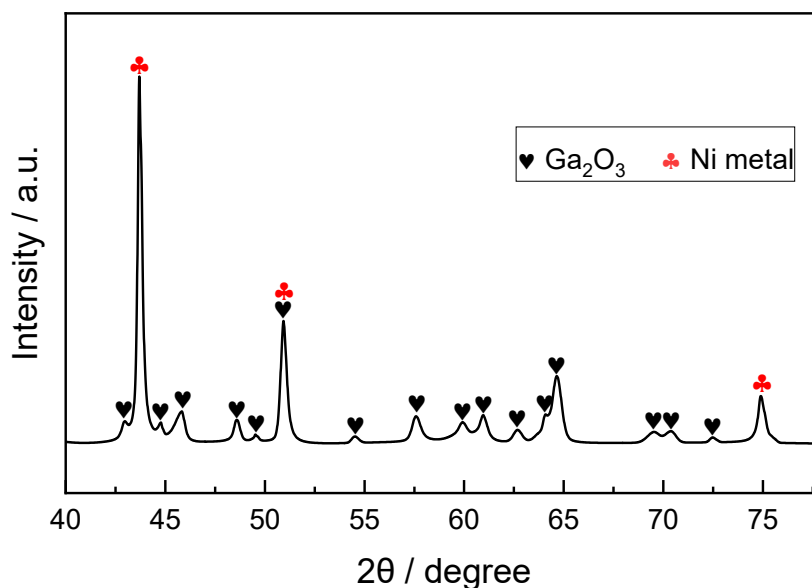
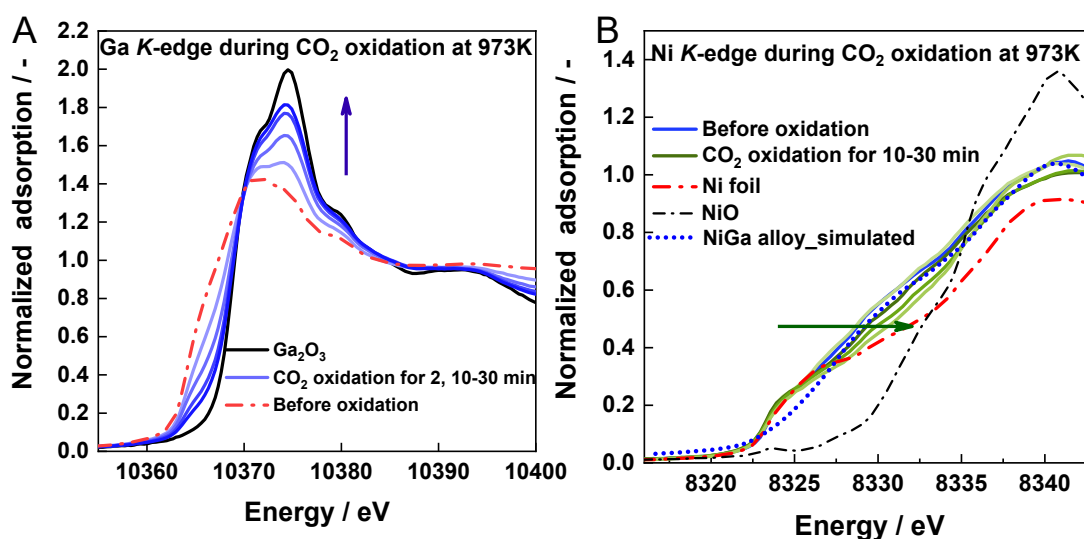Fig. S16 The XRD profiles of $NiGa_2O_x$ after CO_2 oxidation.

Fig. S17 *In situ* XANES spectra of $NiGa_2O_x$ during CO_2 oxidation on (A) Ga *K*-edge, and (B) Ni *K*-edge.

X-ray Absorption Near Edge Structure (XANES) of Ni *K*-edge was simulated to discuss the electronic states of Ni. The experimental and simulated spectra were summarized in Fig. 4C-D and Fig. S17B. A similar pre-edge shoulder peak at around 8330 eV, which can be assigned to *p-d* hybridization between Ga and Ni [*Takayama 2021*], shows up in the spectra of both the after-reduction sample and simulated NiGa alloy. This also manifests that the after-reduction sample shows similar electronic structure with NiGa alloy.

References:

[Takayama 2021] T. Takayama, R. Kariya, Y. Nakaya, S. Furukawa, S. Yamazoe, T. Komatsu, Chem. Commun., 2021,57, 4239-4242
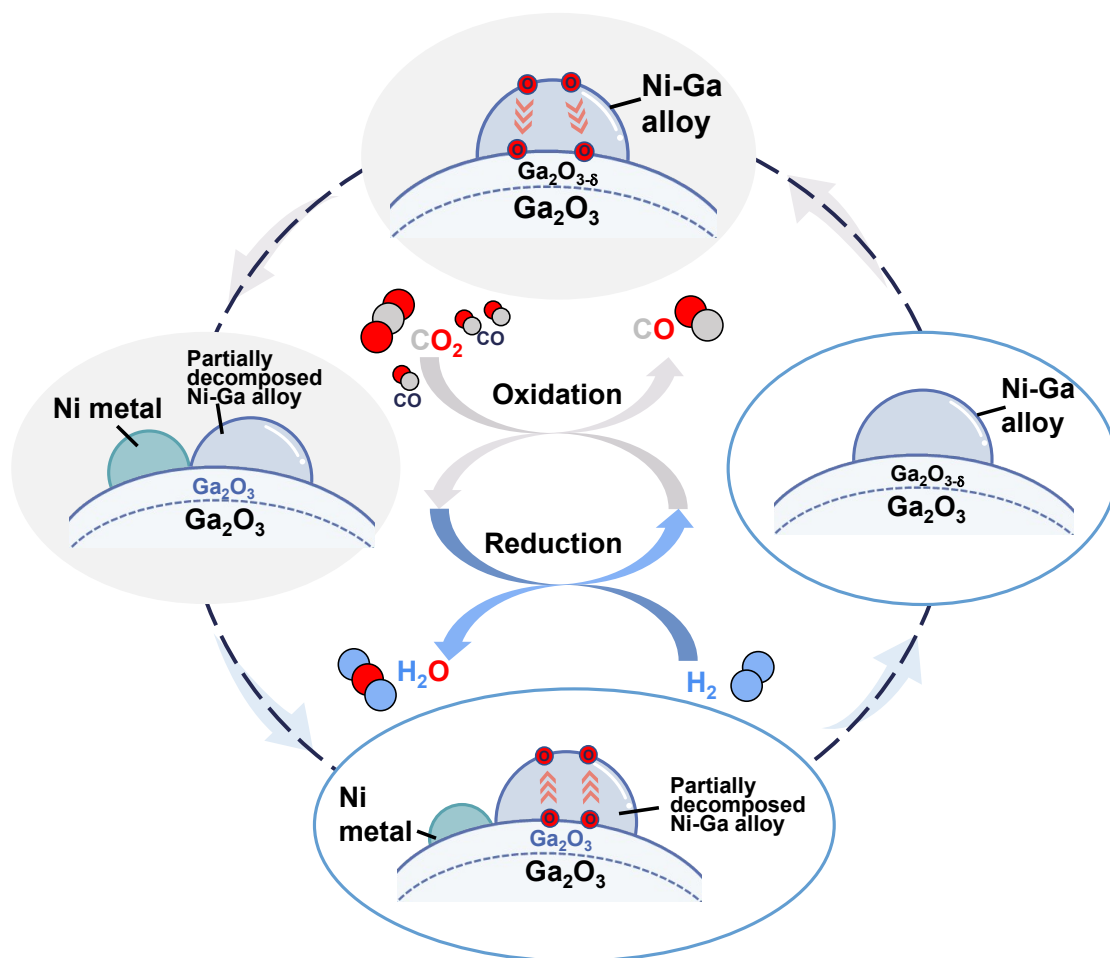
[Takayama 2021] T. Takayama, R. Kariya, Y. Nakaya, S. Furukawa, S. Yamazoe, T. Komatsu, Chem. Commun., 2021,57, 4239-4242

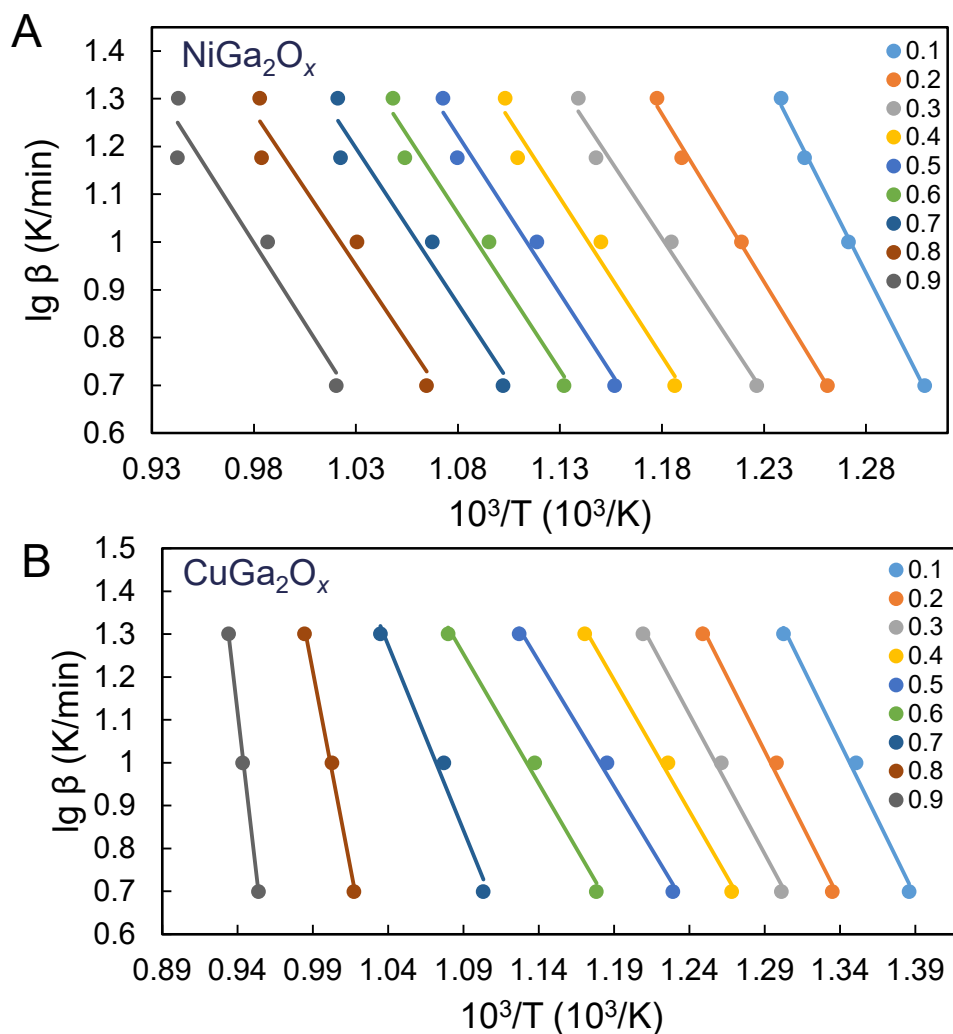Fig. S18 Proposed redox mechanism of $NiGa_2O_x$ during RWGS-CL process.

Fig. S19 Linear plot for determining CO_2 oxidation activation energy calculated by FWO of (A) $NiGa_2O_x$ (B) $CuGa_2O_x$.

Linear plot in Fig. S19 presents the change of CO_2 oxidation conversion (α) with respect to temperature at different heating rates (β), determining CO_2 oxidation activation energy (E_a) calculated by OFW of $NiGa_2O_x$ and $CuGa_2O_x$. Based on this, the activation energy (E_a) of CO_2 oxidation as a function of conversion (α) was obtained and shown in Table S3. Generally, the activation energy of $CuGa_2O_x$ dramatically increases as the conversion increases to higher than 0.6, while the activation energy of $NiGa_2O_x$ keeps stable during the overall process. This illustrates that $NiGa_2O_x$ can keep stable CO_2 oxidation kinetics performance in a wider range than that of $CuGa_2O_x$.
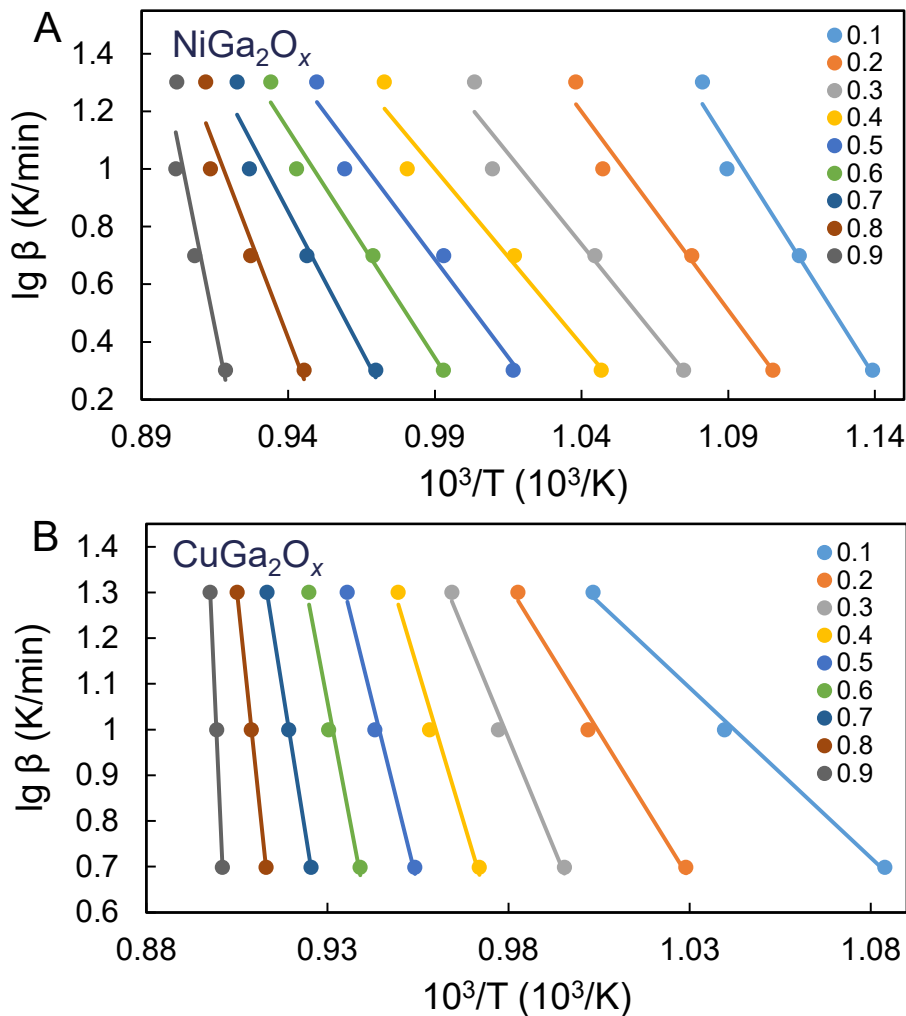
Fig. S20 Linear plot for determining CO reduction activation energy calculated by FWO of (A) $NiGa_2O_x$ (B) $CuGa_2O_x$.

Linear plots for determining CO reduction activation energy calculated by OFW of $NiGa_2O_x$ and $CuGa_2O_x$ are shown in Fig. S20, and Table S4 presents the activation energy (E_a) of CO reduction as a function of conversion (α). The activation energy of $CuGa_2O_x$ is dramatic, manifesting that the performance of $CuGa_2O_x$ is easily influenced by temperature. Regard to $NiGa_2O_x$, the activation energy slightly changes with conversion though, it is generally stable than that of $CuGa_2O_x$. In summary, $NiGa_2O_x$ generally shows more stable activation energy with conversion changing than $CuGa_2O_x$ for both the forward and backward proceeding of the oxidation step (equation 5), which makes $NiGa_2O_x$ a more potential OSM with wider application temperature range even in the presence of high concentration CO than $CuGa_2O_x$.

Table S1 Surface area of MGa_2O_x (M = Ni, Cu, Co) in different reaction stages.

Material	BET surface area at different reaction stages/ $m^2 \, g^{-1}$			
	as made	after reduction	after oxidation	after 5th oxidation
$NiGa_2O_x$	27.3639	7.2308	7.3574	6.0315
$CoGa_2O_x$	17.6798	3.5690	2.1840	1.6865
$CuGa_2O_x$	2.0675	1.8669	0.6092	0.6804

Table S2 Adsorption energy on each adsorption site.

Adsorbate	Catalyst	Adsorption site	Adsorption energy / eV
O adsorption	NiGa	hollow (Ni-Ga-Ga)	-1.76
		hollow (Ni-Ni-Ga)	-1.77
	CoGa	hollow (Co-Ga-Ga)	-1.72
		hollow (Co-Co-Ga)	-2.23
	CuGa	hollow (Cu-Ga-Ga)	-2.02
		hollow (Cu-Cu-Ga)	-2.15
CO adsorption	NiGa	on top (Ni)	-1.08
		bridge (Ni-Ni)	-0.90
	CoGa	on top (Co)	-1.99
		bridge (Co-Co)	-1.71
	CuGa	on top (Cu)	-0.56
CO_2 adsorption	NiGa	physisorption	-0.03
	CoGa	physisorption	-0.04
	CuGa	physisorption	-0.10

Table S3 Activation energy (E_a) of CO_2 oxidation as a function of conversion (α) over $NiGa_2O_x$ and $CuGa_2O_x$.

α	CuGa$_2$O$_x$		NiGa$_2$O$_x$	
	E_a (KJ mol^{-1})	R^2	E_a (KJ mol^{-1})	R^2
0.1	130.36	0.992	153.49	0.997
0.2	126.51	0.993	127.66	0.996
0.3	118.52	0.994	118.17	0.985
0.4	111.54	0.994	120.78	0.971
0.5	106.63	0.993	120.70	0.977
0.6	110.23	0.991	119.53	0.971
0.7	157.57	0.982	118.79	0.951
0.8	333.98	0.995	116.62	0.946
0.9	/	/	122.59	0.944

Table S4 Activation energy (E_a) of CO reduction as a function of conversion (α) over $NiGa_2O_x$ and $CuGa_2O_x$.

α	CuGa$_2$O$_x$		NiGa$_2$O$_x$	
	E_a (KJ mol^{-1})	R^2	E_a (KJ mol^{-1})	R^2
0.1	135.60	0.967	293.51	0.974
0.2	234.20	0.991	250.59	0.971
0.3	349.11	0.990	229.18	0.953
0.4	/	/	222.24	0.959
0.5	/	/	247.22	0.966
0.6	/	/	288.20	0.975